PAPER

Effect of a peripheral substituent on the ultrafast dynamics and the rate of intersystem crossing in the charge-transfer states of platinum(II) acetylides

Iona I. Ivalo, [a] Guanzhi Wu,[a] Rory A. Cowin,[a] Paul A. Scattergood,[a] Tao Cheng, †[a] James D. Shipp,‡[a] Igor V. Sazanovich, [b] Dimitri Chekulaev*[a] and Julia A. Weinstein [a]*[a]

Ultrafast intersystem crossing into a triplet manifold of long-lived charge-transfer states following visible-light excitation is one of the many photophysical features of transition metal complexes that make them attractive for light-harvesting applications. Yet the spin–orbit coupling alone cannot explain the vast differences in the rates of ISC observed in similar transition metal complexes, ranging from sub-100 fs to tens or even hundreds of picoseconds. Here, we investigate how the rate of intersystem crossing and overall excited state dynamics of the two seemingly similar Pt(II) donor–acceptor molecules, Cl–Pt(PBu₃)₂–C≡C–NAP(X), where NAP = naphthalimide, are affected by peripheral changes to the acceptor. The dynamics of the systems was examined using ultrafast broadband fluorescence upconversion spectroscopy (FLUPs), femto-to-microsecond time-resolved infrared spectroscopy (TRIR), and electronic transient absorption spectroscopy (TA). Direct determination of the rate of ISC using FLUPs demonstrated that a change of the N-substituents "X" of the naphthalimide acceptor from an alkyl chain to the aromatic 4-(C(O)OMe)-Ph– group with an IR-active, electron-withdrawing substituent leads to a significant (30%) increase in the rate of intersystem crossing. The contributing factors to such an acceleration are proposed to be a decrease in the energy gap between the singlet charge-transfer state and the triplet manifold, and additional low-frequency vibrational modes associated with the phenyl-ester functional group which may act to promote intersystem crossing. Furthermore, expanding the range of the TRIR measurements into the microsecond timescale using synchronised picosecond excitation and a broad-band mid-IR femtosecond probe allowed us to directly obtain the signatures of long-lived excited states in the mid-IR region, thereby establishing that the final excited state populated in both cases is localised primarily on the acceptor ligand. Overall, this work highlights how the rates of excited state interconversion can be modulated by a seemingly benign peripheral modification.

[a] *Chemistry, School of Mathematical and Physical Sciences, University of Sheffield, Sheffield, UK. E-mail: Julia.Weinstein@Sheffield.ac.uk, d.chekulaev@sheffield.ac.uk*

[b] *Central Laser Facility, Research Complex at Harwell, Rutherford Appleton Laboratory, Harwell Campus, Chilton, Oxfordshire, UK*

† Present address: School of Chemistry and Chemical Engineering, Qilu University of Technology (Shandong Academy of Sciences), China.

‡ Present address: Department of Chemistry, University of Pittsburgh, Chevron Science Center, 219 Parkman Avenue, Pittsburgh, PA 15260, USA.

Introduction

Transition metal complexes have been widely studied in light-driven processes due to the strong absorption of visible light and the almost unlimited possibilities of metal–ligand design combinations.[1–6] An essential step in many applications, including solar light harvesting,[2,7] photocatalysis,[8,9] or optoelectronics,[10–16] is photoinduced charge separation, leading to the formation of a charge separated state (CSS).[17,18] In this regard, a desirable property of transition metal complexes is the presence of the lowest energy state of the charge transfer character, such as metal-to-ligand or ligand-to-ligand charge transfer.[19] The requirement to form a charge-separated state implies the construction of molecular B–A dyads, D–B–A triads and more elaborate architectures, where D is an electron donor, A is an electron acceptor, and B is a bridge connecting the two moieties.

Pt(II) complexes in which a D and an A unit are positioned across the platinum centre in a linear manner are especially interesting due to the directionality of the electron transfer process that they offer.[20–26] *trans*-Diphosphine Pt(II) complexes

This journal is © the Owner Societies 2025

Phys. Chem. Chem. Phys., 2025, **27**, 25825–25836 | **25825**

have been amongst the most studied groups of such systems for potential applications in photocatalysis and optoelectronic devices.[10–16]

A particular advantage of transition metal complexes over organic systems lies in the strong spin–orbit coupling (SOC) of the heavy central atom, which leads to efficient, ultrafast intersystem crossing from the initially populated manifold of singlet excited states into the triplet manifold. The lowest excited state thus becomes a triplet state, with the excited state lifetime increasing from a few nanoseconds to hundreds of nanoseconds or even microseconds due to the spin-forbidden nature of its decay to the ground singlet state.[27,28] Surprisingly, the range of ISC timescales reported for Pt(II) acetylides spreads over at least four orders of magnitude, from 15 fs to 193 ps.[1,20,29–43] An invocation of the SOC alone cannot account for such a vast variation in the timescales of this process, and hence the mechanism of ISC in Pt(II) complexes including the role of low-frequency vibrations[44–47] remains an important question.

The Pt(II) acetylide complexes of strong electron acceptors, such as naphthalimide and its derivatives, possess both a brightly emissive, fluorescent state and a long-lived, phosphorescent state,[48–52] and thus can be an excellent testing ground for understanding what other factors, apart from SOC, influence the rates of ISC. Here, we investigate how a subtle change of the substituent on the N-atom of the naphthalimide[29,49] from $-C_8H_{17}$ to an aromatic ester group, p-methyl benzoate (–PhCOOMe), significantly impacts the rate of intersystem crossing (Fig. 1). One of the motivations here is, in the long term, to use carboxy-substituents as a means to anchor D–Pt–A to photoactive surfaces.

The excited state dynamics of the Pt(II) D–B–A complexes has been investigated by a combination of electronic and vibrational methods. Importantly, broadband femtosecond fluorescence upconversion spectroscopy (FLUPs) allowed us to follow the intersystem crossing process in real time. The FLUPs studies were complemented by femtosecond transient absorption (TA) spectroscopy in the UV/vis and NIR regions. Time-resolved infrared (TRIR) spectroscopy in the mid-IR allowed for localisation of the excited state to be inferred by observation of transient vibrational signals of acetylide, imide, and ester IR-reporting groups positioned along the molecular axis. We further employ our newly established microsecond TRIR set-up (picosecond excitation/femtosecond probing) to ascertain the IR-signature of the final excited state. Taken together, the results of these methods help understand how the process of

ISC is influenced by subtle changes in the structure of D–Pt–(C≡C)–A systems, and emphasize that the ancillary group on the imide, usually incorporated for practical reasons such as to tune solubility or to enable attachment to surfaces, cannot be considered an "innocent bystander".

Results and discussion

The ground-state absorption spectra of the two complexes in CH_2Cl_2 solution (Fig. 2(a)) exhibit two key spectral features: a broad band in the 400–440 nm region due to a metal-to-ligand charge transfer (MLCT) transition from the Pt(II)–acetylide unit to the naphthalimide ligand,[49,50] and strong absorption features towards the UV range from 300 nm due to ligand-centred (LC), $\pi \rightarrow \pi^*$ transitions. The MLCT band centred at 424 nm in complex A[49] is slightly shifted toward lower energies in B, i.e., to 434 nm. The positions of the absorption bands are in good agreement with the calculated band positions obtained through time-dependent density functional (TD-DFT) calculations, where the lowest singlet state is predicted to absorb at 432.5 nm and is of MLCT character (Fig. S10 and Table S5). The shape of the MLCT band at 434 nm indicates the presence of multiple transitions overlapping each other and is also consistent with the TD-DFT results that predict a second transition at 410.7 nm. The difference in energy for the MLCT transitions in A and B is 0.067 eV, which is close to the observed $\Delta E = 0.08$ V difference in the electrochemical potential of the first reduction process that is localised on the naphthalimide ligand ($E_{1/2}^{red} = -1.83$ V and -1.75 V for A and B, respectively; Fig. S1).

The emission spectra (Fig. 2(b)) of both complexes in a solution of CH_2Cl_2 exhibit a broad emission band centred at 493 nm for A and at 502 nm for B; the broad structureless emission is assigned to an MLCT state with singlet character. Under an inert atmosphere, the emission spectra of both complexes show a second, structured emission band between 600 and 750 nm, which is characteristic of phosphorescence from a triplet state localised on –CC–naphthalimide (^3NAP).[48,51,53] Both the fluorescence and phosphorescence spectra of B are slightly redshifted with respect to A (Fig. 2(b)).

The studied complexes contain several spectrally and positionally different functional groups along the molecular axis that can act as IR-reporters in ultrafast TRIR spectroscopy measurements.[54] IR band assignments for complex B shown in Fig. 2(c) are based on DFT frequency calculations (see
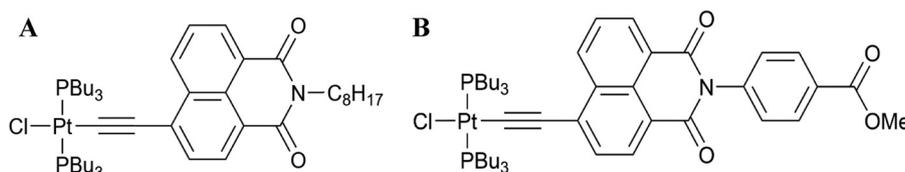

Fig. 1 Chemical structures of the reference compound Cl–Pt–NAP (A) and that with the N-alkyl replaced by an N-Ph-ester substituent, Cl–Pt–NAP(PhCOOMe) (B) investigated in this work. Synthetic details and characterisation are provided in the SI.
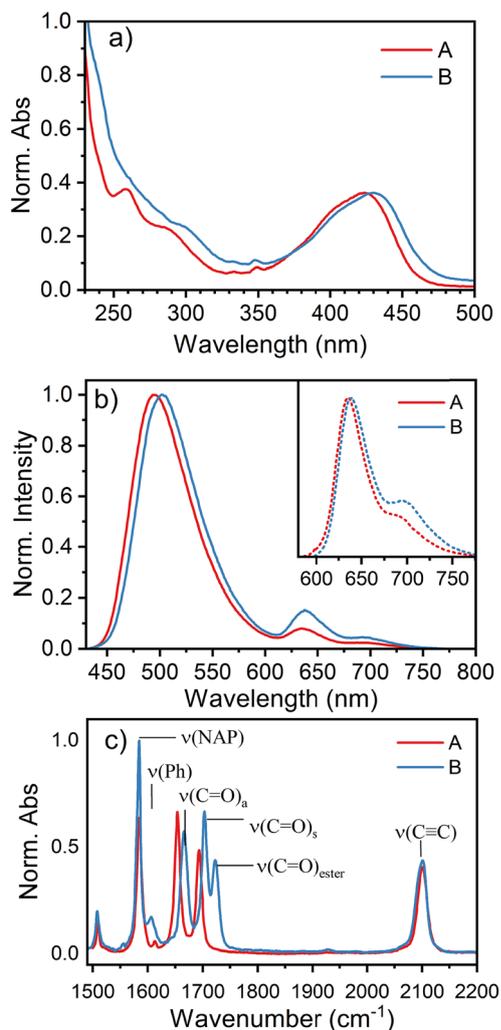
25826 | Phys. Chem. Chem. Phys., 2025, **27**, 25825–25836

This journal is © the Owner Societies 2025

Fig. 2 Absorption, emission and FTIR spectra of complexes **A** and **B** in CH$_2$Cl$_2$. (a) Absorption spectra. (b) Emission spectra recorded in deaerated solutions showing fluorescence (450–600 nm) and phosphorescence (600–750 nm) emissions. The inset shows an expanded view of the phosphorescence spectra, recorded using the phosphorescence mode of a Cary Eclipse spectrofluorometer. (c) Fourier-transform infrared (FTIR) spectra, with the vibrational modes of complex **B** labelled.

Section 6 in the SI) and match those of complex **A**, which have been discussed previously.[49] For both **A** and **B**, the acetylide band ν(C≡C) appears at 2100 cm^{-1} and is spectrally isolated from the other vibrational modes. Several characteristic vibrations are also present in the 1500–1730 cm^{-1} region. The bands at 1665 and 1702 cm^{-1} are attributed to asymmetric ν(C=O)$_a$ and symmetric ν(C=O)$_s$ combinations of stretching vibrations of the carbonyl groups in the naphthalimide, respectively; these modes are slightly shifted to higher frequencies in **B** vs. **A** as a result of an electron-withdrawing ester group. The ester carbonyl stretch located on the aromatic ester end-group, hereafter ν(C=O)$_e$, has an absorption at 1721 cm^{-1}. The remaining vibrational modes in this region, at 1585 and 1602 cm^{-1}, arise from aromatic ring vibrations in naphthalimide (ν(NAP)) and the phenyl rings (ν(Ph)), respectively.

Fluorescence upconversion spectroscopy

Femtosecond fluorescence upconversion spectra of complex **B** were recorded following excitation at 400 nm in CH$_2$Cl$_2$ solution. The emission spectrum of **B** (Fig. 3) shows a band initially centred at 479 nm, which red-shifts to 502 nm. Dynamic shifts in the fluorescence wavelength are typically related to fast solvation processes of the initial excited states[55,56] convoluted with structural changes, and we assign the 23 nm shift (956 cm^{-1}) to similar processes occurring in **B**. In complex **A**, the emission maximum after the spectral shift is complete is located at 494 nm.[29] In both cases, the final emission wavelength matches that observed in the steady-state emission spectrum. Therefore, the FLUPs data confirm that the modification of the acceptor end-group from an alkyl group to a slightly more electron-withdrawing –Ph–COOMe group has shifted the fluorescent state to lower energies, consistent with the differences in the absorption maxima and the first reduction potentials between **A** and **B**.

The dynamics observed in the FLUP spectra were fitted using a global model with three parallel components, which yielded time constants of 1 ps, 8.2 ps, and 131 ps. We note that the calculated errors obtained from the global fitting procedure are especially small (see the SI for details) and are simply the error of the fitting parameters; therefore, the instrument response of this set-up, 150 fs, is assumed as a realistic error. Whilst the data were modelled with discreet time constant values, the spectra demonstrate a gradual shift that cannot be modelled by global fitting. Therefore, we treat the individual values of 1 and 8.2 ps as approximate timescales of solvation, reorganisation and relaxation within the singlet excited state manifold. It has been demonstrated that ISC occurs over a multitude of timescales in such systems,[29] and thus the early-time FLUPs dynamics also reflects the continuous evolution of the excited state from singlet to triplet multiplicity on a timescale of up to 131 ps (Fig. 3).

Ultrafast transient absorption in the UV/vis-NIR region

The nature and dynamics of the electronic excited state of complex **B** were further investigated by femtosecond transient absorption spectroscopy, across the UV to NIR regions, following photoexcitation of the MLCT transition at 400 nm (Fig. 4 and 5).

Firstly, in the UV-vis region, immediately following photoexcitation, a depletion of the ground state absorption of the MLCT band is evidenced by the bleach at 425 nm (Fig. 4a). Superimposed upon this bleach is excited state absorption (ESA) with a maximum at 470 nm, which is a characteristic of the naphthalimide anion[57] NAP$^-$; the intensity of this band increases over several picoseconds. Simultaneously, a second negative band present at 515 nm increases in intensity on the same timescale, which can be attributed to stimulated emission from the charge-transfer states. The 515 nm band is assigned to the same fluorescence as the emission band detected in FLUPs measurements at 503 nm. The apparent shift is caused by an overlap with the positive ESA in the TA measurements; the

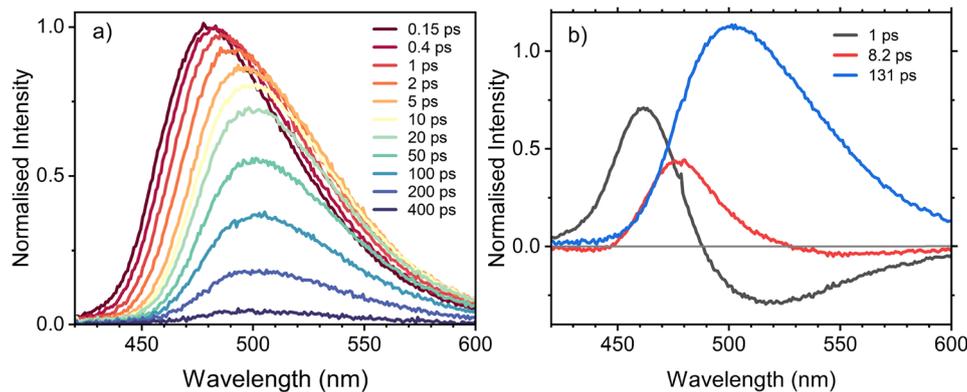This journal is © the Owner Societies 2025

Phys. Chem. Chem. Phys., 2025, **27**, 25825–25836 | **25827**

Fig. 3 Fluorescence upconversion spectra of complex **B** in CH$_2$Cl$_2$ solution following photoexcitation at 400 nm. (a) Experimental spectra at selected time-points. (b) Decay-associated spectra (DAS) obtained from global lifetime analysis using a parallel model with three components, as stated on the graph. See the text for details of the parameters/errors.

decay associated spectra show SE at approximately 502 nm. The simultaneous increase in the observed amplitude of the NAP$^-$ ESA and the SE band peaks is attributed to the same fast relaxation processes as were observed by FLUPs, where the dynamic shift in the fluorescence wavelength leads to reduced mutual cancellation of the positive and negative spectral features. The final spectrum observed from *ca.* 130 ps can be assigned to a triplet state localised on naphthalimide, ^{3}NAP, based on its spectral shape, and the lack of further evolution observed up to the final time delay of the experiment at 6 ns. The UV-visible transient absorption features of complex **A** have been discussed extensively in previous work.[29,49] The spectral features are very similar to those of complex **B** (see Fig. S2 for a direct comparison), but the kinetic behaviour differs between the two complexes (see below).

Of particular interest is the previously unexplored near-infrared (NIR) region of the excited state absorption, which is important as it provides an insight into the manifold of singlet and triplet low-lying excited states, which could potentially determine the rate of ISC (Fig. 5). At early times, the NIR spectra of **B** show a broad, slightly structured ESA. A broad positive offset observed in the NIR spectra that extends into the mid-IR region (see the early-time TRIR data) is characteristic of the oxidised [Pt-CC] fragment of the MLCT excited states of Pt(II) acetylides.[24,26,58–62] Superimposed on this offset are a broad peak at 925 nm and a shoulder at 1125 nm, which shift on a timescale of *ca.* 130 ps to 1000/1155 nm ($\Delta E = 1341$ cm^{-1}). This spectral shift is concomitant with the decay of the broad offset, thus reflecting the transition from a "$^-$NAP-[CC-Pt]$^+$ CT" state to an intra-ligand π–π^* state localised on the acceptor, ^{3}NAP.[49] No further changes in the spectral profile occur up to the final time delay of 6 ns.

In the NIR region, complex **A** shows the same spectral features (Fig. 5) albeit at shorter wavelengths, with respect to complex **B**. The structured bands at early times appear at 900 and 1125 nm and shift during the formation of the final triplet state to 993 and 1146 nm ($\Delta E = 1345$ cm^{-1}). The differences in the spectra of **A** and **B** in the NIR range are very small, with the vibronic progression being virtually identical for

A and **B**, confirming the similar nature of the absorbing state and its localisation on the NAP moiety.

A global analysis of the TA data was performed using a four-component parallel decay model, obtaining the following time constants: $\tau_1 = 0.93$ (± 0.006) ps, $\tau_2 = 12.2$ (± 0.2) ps, $\tau_3 = 131$ (± 0.15) ps, and a final constant value (see above the comment regarding the errors here being purely fitting errors; the IRF is ~150 fs). The time constants obtained from the NIR data were $\tau_1 = 0.95$ (± 0.05) ps, $\tau_2 = 20.8$ (± 2) ps, $\tau_3 = 131$ (± 0.15) ps, and a constant. The initial 0.9 ps component is very similar to the first time constant obtained from the FLUPs data and is thus also attributed to relaxation of the initial states, convolved with the solvent relaxation. In the TA spectra, this time constant is also associated with a blue shift of the ESA at 470 nm, indicating that vibrational cooling also contributes to the fast relaxation processes.

Time-resolved infrared spectroscopy

Time-resolved infrared measurements were performed with 400 nm photoexcitation and a mid-IR probe on a CH$_2$Cl$_2$ solution of **B**. Initial excitation resulted in a ground state bleach of the ring modes, carbonyls and the acetylide modes in the spectrum, as shown in Fig. 6(c) and (d). In the carbonyl and aromatic regions, positive signals are present at frequencies of 1501, 1565, and 1625 cm^{-1} immediately following photoexcitation (Fig. 6(c)). These signals are indicative of rapid formation of the naphthalimide anion, NAP$^-$, which has been observed by IR-spectroelectrochemical studies in similar complexes.[57] On a 120–150 ps timescale, the NAP$^-$ transients decay, whilst simultaneously positive signals grow at frequencies of 1602, 1647 and 1969 cm^{-1}, which are characteristic of ^{3}NAP.[49,57] The timescale of NAP$^-$ decay in the TRIR data matches the rates observed in the NIR TA data, confirming our assignment of the peaks in the 900–1300 nm region to the CT and ^{3}NAP states. Importantly, ^{3}NAP features are already present from early times, which indicates some of the species undergo ISC directly from the initial charge transfer state (as has been discussed in detail for complex **A**[29]); however, the bulk population is not achieved until *ca.* 500 ps – consistent with our interpretation of
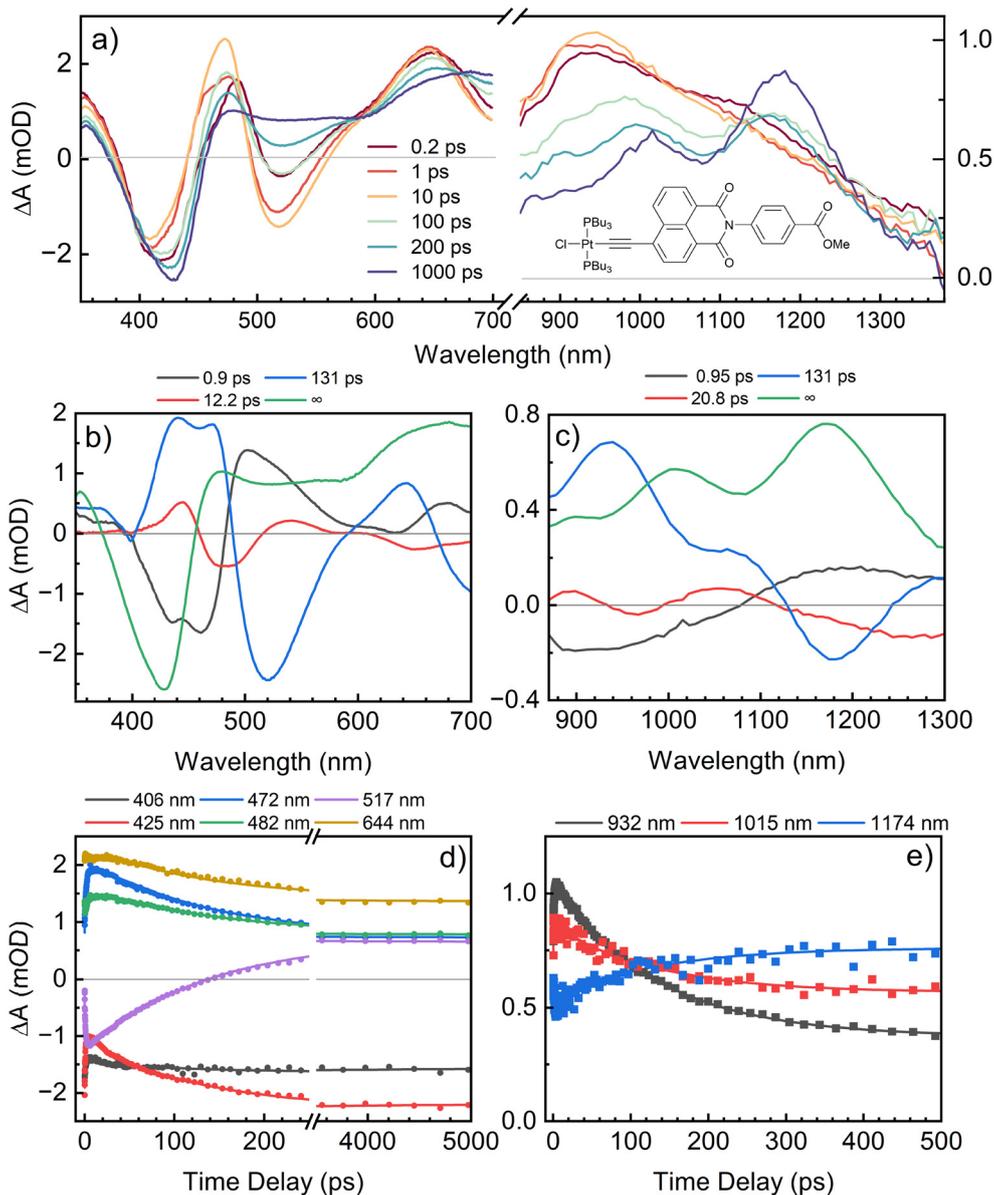
25828 | *Phys. Chem. Chem. Phys.*, 2025, **27**, 25825–25836

This journal is © the Owner Societies 2025

Fig. 4 (a) Transient absorption spectra of complex **B** in CH_2Cl_2 solution, in the UV to NIR region, obtained under photoexcitation at 400 nm. (b) and (c) Decay-associated spectra acquired from global analysis of TA data fitted with four parallel components. (d) and (e) Kinetic traces and the multiexponential fit to the data at selected wavelengths of key features shown.

the FLUPs and TA spectra. In the acetylide region 1900–2200 cm^{-1}, we observe a broad offset following photoexcitation. The intensity of the offset is greater towards higher energies – consistent with the assignment of this feature to the tail of an absorption of the charge-transfer electronic excited state that is observed across the mid-IR, NIR and visible regions. A small peak was identified 29 cm^{-1} higher in frequency than the ^{3}NAP peak at 1998 cm^{-1} (as observed in the DAS in Fig. S5, which grows in with the initial signal before disappearing by *ca.* 200 ps). The IR spectra of the S_1 and T_1 excited states simulated by frequency calculations at the optimised excited state geometries predict a 39 cm^{-1} difference between ν(CC) in these states which is close to the experimental value. The difference

from the experimental value of the $\Delta\nu$(CC) could be attributed to the calculations being performed in the harmonic approximation, whilst in the experiment the 400 excitation could populate a mixture of S_1/S_2 states, Table S5). Therefore, we attribute the small peak at 1998 cm^{-1} at the early times to the acetylide vibration of the nascent excited state(s).

It is likely that the initially populated manifold of singlet CT states undergoes intersystem crossing into both T_2, a ^{3}MLCT state, as well as T_1, which has ^{3}NAP character (Fig. S10). If populated, the ^{3}MLCT state will extremely rapidly populate ^{3}NAP by internal conversion. The 1998 cm^{-1} band could alternatively be a signature of the ^{3}MLCT state, which will not be easily detectable in the carbonyl region, where the IR spectrum

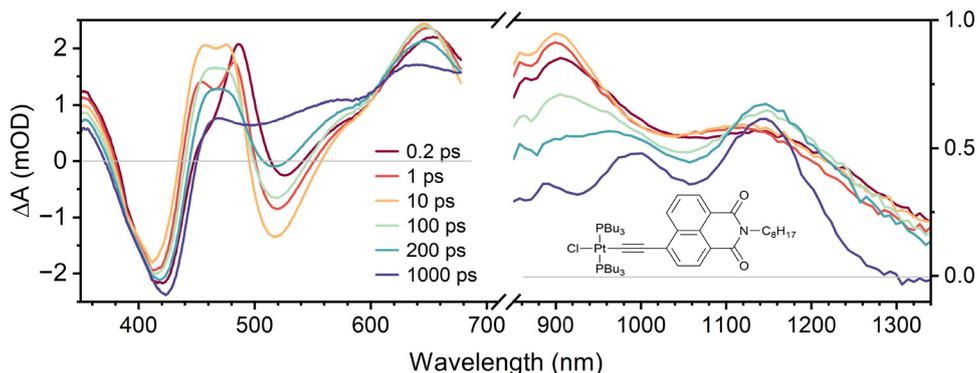This journal is © the Owner Societies 2025

Phys. Chem. Chem. Phys., 2025, **27**, 25825–25836 | **25829**

Fig. 5 Transient absorption spectra of complex **A** in the UV-to-NIR region obtained from photoexcitation at 400 nm in CH$_2$Cl$_2$ solution (time delays stated in the figure).
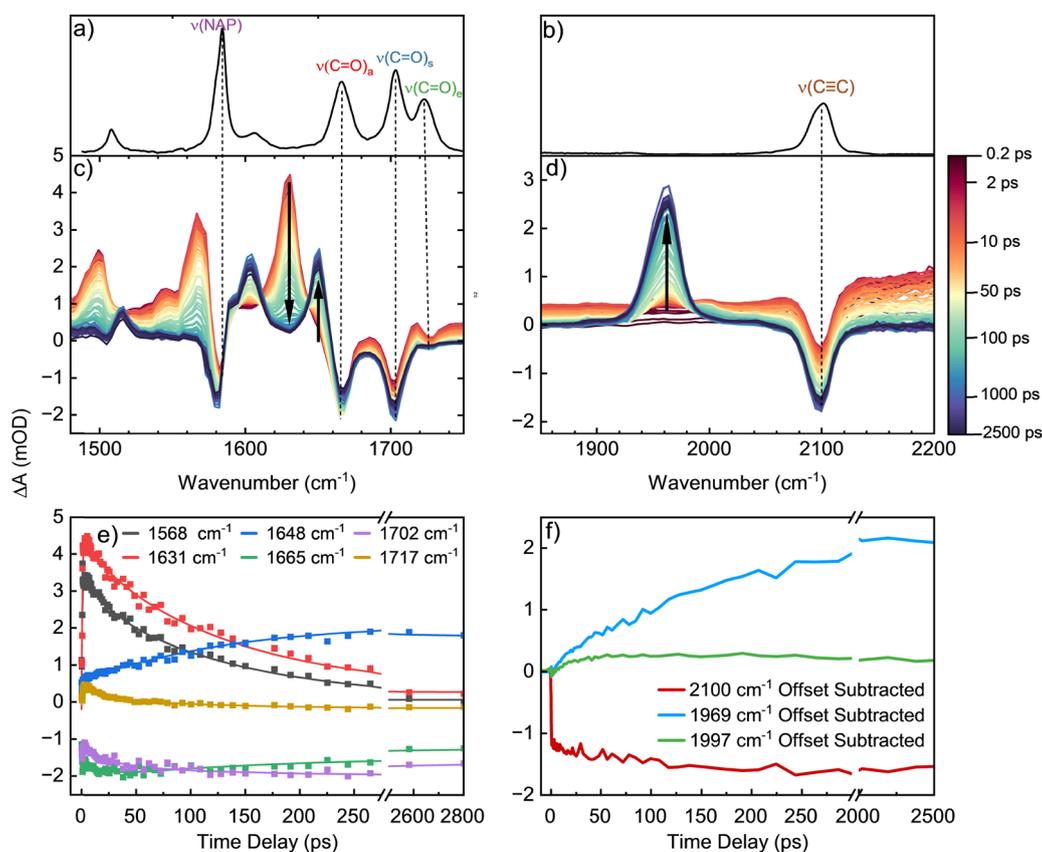

Fig. 6 FTIR spectra (a), (b), time-resolved infrared spectra (c), (d) and kinetics (e), (f) for complex **B**. TRIR spectra were recorded following photoexcitation at 400 nm, in CH$_2$Cl$_2$ solution with an initial and a final time delay of 0.2 (red) and 2500 ps (indigo), respectively. The data are shown in (a), (c) for the 1500–1750 cm^{-1} region and in (b), (d) for the acetylide region (150–2200 cm^{-1}). (e) Kinetic traces at key spectral positions. Solid lines indicate the fit to the data with multiexponential function using the following time components: $\tau_1 = 0.7 \pm 0.02$ ps, $\tau_2 = 20.8$ ps, $\tau_3 = 131$ ps and $\tau_4 =$ constant. (f) Kinetic traces of the GSB (2100 cm^{-1}), the growth of ^{3}NAP (1969 cm^{-1}), and the feature at 1997/8 cm^{-1}. Note that the electronic offset at 2050 cm^{-1} has been subtracted to extract the true kinetic behaviour of the vibrational features.

of the ^{3}MLCT state would be very similar to that of the ^{1}MLCT. The spectroscopic data are thus consistent with both cases, where the singlet CT states undergo ISC on a 131 ps timescale to either populate ^{3}NAP directly or a rapidly decaying ^{3}MLCT state that is not easily observed due to its short lifetime – this is

consistent with the previous interpretation of the ISC process in compound **A**.[29]

The 3rd component of the TRIR spectral evolution occurs with a time constant of 131 ps, with the final TRIR spectral shape persisting beyond the longest time delay of 2.8 ns. The

25830 | *Phys. Chem. Chem. Phys.*, 2025, **27**, 25825–25836

This journal is © the Owner Societies 2025

peaks at 1725 and 1714 cm^{-1} are attributed to ester carbonyl GSB and ESA bands. The presence of the ester carbonyl in the TRIR signal suggests that the electron density is delocalised across naphthalimide and the N–Ph–COOMe unit upon photo-excitation and subsequent population of the triplet state, causing a small change in the C=O vibrational frequency. Global analysis using four exponential functions in a parallel model in the carbonyl region gave the following fit parameters: τ_1 = 0.61 ps, τ_2 = 20.8 ps, τ_3 = 131 ps and a constant, whilst for the acetylide region the fit parameters were τ_1 = 0.70 ps, τ_2 = 24.1 ps, τ_3 = 131 ps (fixed to the value extracted from FLUPs measurements) and a constant. The first two time constants obtained by fitting of the TRIR spectra are in good agreement with those found through TA and FLUPs as previously discussed. Changing the excitation wavelength from 400 nm to 420 nm in the TRIR experiments did not affect the spectral shape or dynamics, as shown in Fig. S7.

Charge density difference isosurfaces were plotted from the output of the TD-DFT calculations to show how electron density is redistributed upon vertical excitation from the ground state to the first four singlet or triplet excited states (Fig. S10). The change in electron density upon transfer from S$_0$ to T$_1$ indicates a small involvement of the ester-Ph group in the T$_1$ excited state. The first unoccupied orbital that involves the –PhCOOMe group is LUMO+1, as visualised in Fig. S9. TD-DFT results indicate that the lowest energy vertical excitations that involve this LUMO would be of S$_7$ and T$_6$ character, occurring at 304 nm and 334 nm, respectively (see Tables S5 and S6), which lie considerably higher than the excitation energy of 3.1 eV (400 nm) used. Therefore, at the current level of theory, TD-DFT predicts little direct involvement of the ester group in the excited states, which are accessible following 400 nm excitation. However, the TRIR differential signals observed in the ester region indicate that the ester–Ph group is nonetheless sensitive to the changes in electron density on the naphthalimide ligand. To confirm this, we simulated the TRIR spectrum of the S$_1$ and T$_1$ states by first optimising the geometry of S$_0$, S$_1$, and T$_1$, and then calculating the vibrational normal mode frequencies under harmonic approximation (Fig. S11). The frequency of the ester carbonyl mode has a small, predicted shift (0.7 cm^{-1}), which was significant enough to produce an ESA/GSB pair in the simulated data.

Thus, despite the electron density maps of the frontier orbitals not showing direct involvement of the ester groups, there is nonetheless a small change in the $\nu(CO)_e$ frequency upon population of the singlet or triplet excited states. This indicates that the involvement of the –PhC(O)OMe group is minimal in terms of hosting electron density following photo-excitation and instead its main impact is changing the electron-accepting ability of the naphthalimide. The small shift in $\nu(CO)_e$ in the excited states indirectly reflects the change of electron density of the naphthalimide core in the excited state. The simulated spectra predict a higher intensity of the $\nu(CO)_e$ signal in S$_1$ compared to T$_1$, which could result from an increased calculated participation of the Ph ring in the charge density difference of the singlet state (Fig. S9).

The results from the multiple methods described above determine the rate of ISC for **B** occurring on a timescale of up to 131 ps, which is significantly faster than that for **A** (193 ps),[29] albeit still orders of magnitude slower than one would have anticipated from the general considerations of the strength of SOC in Pt(II) complexes. The contributing factors for such an acceleration of the ISC process in **B** vs. **A** may include a slight decrease in the energy gap between the nascent singlet states and the triplet manifold increasing transition probability. The decrease in the energy gap between vertical S$_0 \rightarrow$ S$_1$ and S$_0 \rightarrow$ T$_1$ transitions was estimated through TD-DFT calculations of **A** and **B**, obtaining a value of 201 cm^{-1} (see Fig. S10 and Tables S5, S6). The energy gap between the relaxed S$_1$ and T$_1$ states was smaller (93 cm^{-1}), but still evident in the calculations. Further, we hypothesise that additional lower-frequency vibrational modes associated with the Ph–ester group may facilitate ISC between singlet and triplet manifolds. We have identified several example modes that are primarily localised on the Ph–ester moiety in the harmonic frequency calculations of both the relaxed S$_1$ and T$_1$ states of **B** at 1560 (Ph stretch), 1343 (C–O stretch), 1176 (Ph C–H bend), 1162 (Ph stretch), 1114 (Ph stretch), 1042 (Ph stretch) and 320 cm^{-1} (R–O–C=O bending). Considering previous 2DIR spectroscopy studies of **A**,[63] we expect these modes to be anharmonically coupled to other low-frequency modes, which could also act to promote ISC.

The contributions of the NAP, ester, and Pt fragments of **B** to the first two singlet (S$_0 \rightarrow$ S$_1$ and S$_0 \rightarrow$ S$_2$) and two triplet (S$_0 \rightarrow$ T$_1$ and S$_0 \rightarrow$ T$_2$) transitions were visualised using the molecular orbitals obtained by TD-DFT (Fig. S8). For all four of these transitions, the electron density acceptor was the LUMO, centred at the NAP π-system. The orbitals donating electron density in the vertical transitions were the HOMO and HOMO−1 for the S$_1$, S$_2$, and T$_2$ transitions. Both the HOMO and HOMO−1 have contributions from the Pt–CC centre and the NAP ring, and thus these transitions can be characterized as having a mixed MLCT and π–π* character. The T$_1$ transition has a similar orbital parentage to T$_2$, but had an additional contribution from HOMO−4, which also has the involvement of the Pt–CC and NAP groups. For S$_1$ and T$_1$, the largest orbital contribution is from HOMO → LUMO, whilst for excitations to S$_2$ and T$_2$, HOMO−1 → LUMO was the greatest contributing orbital transition (Table S2).

The percentage contribution of the Pt centre to these molecular orbitals was found to change upon the addition of the ester-Ph group to the NAP ring (Table S3). The Pt contribution to HOMO−1 decreases from 34.5% to 32.2%, whilst the contribution to the HOMO increases from 15.3% to 17.7%. The Pt contribution to the LUMO is very similar in both complexes, slightly increasing by 0.14%. Considering the closest energy transition to our excitation wavelength is S$_0 \rightarrow$ S$_2$ and 62% of this transition is composed of HOMO−1 → LUMO, the decreased contribution of the Pt atomic orbitals to HOMO−1 could partially explain the observed slower rate of ISC, as was shown previously for some systems.[64] However, this does not take into consideration the increased Pt contribution to the HOMO, which is the largest contributor to the S$_0 \rightarrow$ S$_1$ transition.
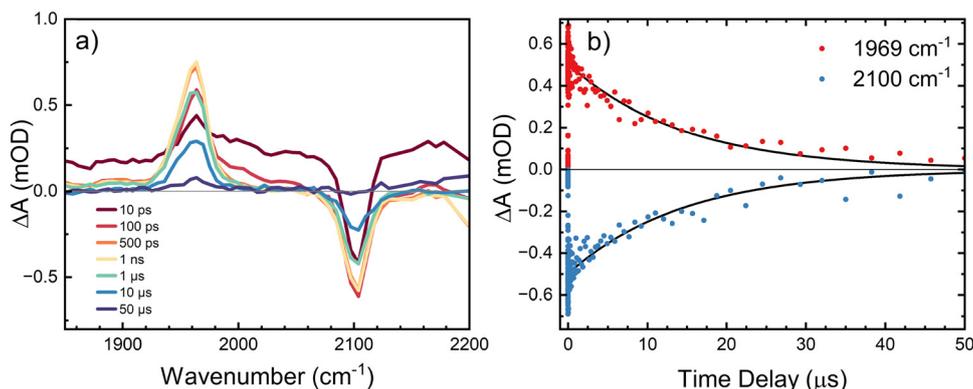
This journal is © the Owner Societies 2025

Phys. Chem. Chem. Phys., 2025, **27**, 25825–25836 | **25831**

Fig. 7 (a) Microsecond time resolved infrared spectrum of a CH_2Cl_2 solution of complex **B** following 400 nm excitation at selected time delays. (b) Kinetic traces of the GSB at 2100 cm^{-1} and the triplet ^{3}NAP at 1969 cm^{-1} including a solid line denoting the monoexponential fit of the long-time dynamics, with a time component of 14.5 ± 0.9 μs (note that the lifetime is oxygen- and concentration-dependent).

Microsecond time-resolved broadband infrared spectroscopy

In order to obtain the spectra of the final excited state and also to follow the decay dynamics with a transient spectroscopy method (in addition to emission decay), we set up a TRIR system where the detection (probe) pulse can be delayed from the excitation pump pulse in the microsecond range. To achieve this, two amplifiers were synchronised: a 5-ps 400 nm excitation pulse from a 5 kHz amplifier was synchronised with a 100-fs probing pulse from a 10 kHz amplifier. The experiment was performed using a combination of an optical delay line and an electronic delay generator (see the Experimental section for details). Measurements were performed on complex **B** at room temperature in the presence of O_2 (OD of 0.3 at 400 nm, pathlength of 650 μm, approx. 0.11 mM) (Fig. 7).

The transient IR-absorption signal of ^{3}NAP at 1969 cm^{-1} has the same shape and grows on the same timescale as observed in ps-TRIR measurements reaching a maximum at *ca.* 500 ps. The broad offset of the signal observed across the entire spectral region decays by ∼500 ps. The transient signal of the ^{3}NAP triplet state decays concomitantly with the ground state bleach recovery at 2100 cm^{-1}. These data confirm that the ^{3}NAP state is the lowest excited state in this molecule, with no further

evolution or population of long-lived non-emissive states. The lifetime for ^{3}NAP in **B**, under the stated environmental conditions, was determined from the tail of the decay from 1 ns with a single exponential function as 14.5 ± 0.9 μs. It should be noted that the lifetime of the lowest excited state in such type of complexes is dependent on the presence of O_2, temperature, and the concentration of the sample (and that, depending on the conditions, ^{3}NAP can have a lifetime of hundreds of microseconds).[57,65]

Conclusions

The effect of the modification of the charge-accepting ligand in a Pt(II) acetylide–acceptor complex on the overall photophysical properties, and specifically on the rate of intersystem crossing, has been investigated. This question was addressed using a combination of ultrafast broadband fluorescence upconversion (FLUP) spectroscopy to detect singlet states directly, with femtosecond TA (UV/Vis–NIR range), femtosecond TRIR, and microsecond TRIR to follow the dynamics of the excited states, with the resulting energy level diagram and time scales summarised in Fig. 8. We also report the first near-IR absorption spectra of the –Pt–C–≡–C–NAP systems, as well as the IR signature of the ^{3}NAP state (Fig. 5).

The change of an alkyl substituent on the naphthalimide ligand to a more electron-withdrawing methyl benzoate group led to a slight shift in the energy of the MLCT absorption transition, mirrored by the shift in the fluorescence maximum, and matching the difference in the 1st reduction potentials of **A** and **B** of about 0.07 eV. The key spectral features in the two complexes are the same; however, the excited state evolution occurs on different timescales. This suggests that the substituent on the N-atom, whilst perceived as an "innocent" group, does nonetheless participate in the electronic states and contributes to their dynamics by increasing the electron-accepting ability of naphthalimide, lowering the energy of the CT manifold, and changing the landscape of low-frequency modes contributing to the ISC reaction coordinate.
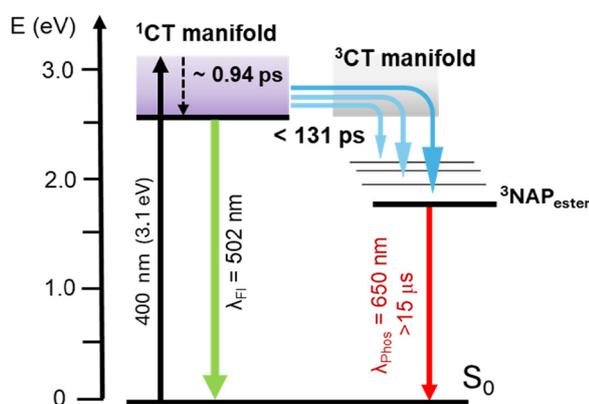

Fig. 8 A simplified energy level diagram for compound **B** – Cl-Pt-NAP-(PhCOOMe).

25832 | *Phys. Chem. Chem. Phys.*, 2025, **27**, 25825–25836

This journal is © the Owner Societies 2025

Specifically, a broad range of time-resolved spectroscopic methods established that the rate of intersystem crossing in Cl–Pt–C≡C–NAP–PhCOOMe from the singlet CT manifold occurs on a time scale of up to 131 ps. The notable (30%) acceleration of ISC in complex **B** relative to **A** (193 ps, an alkyl substituent) cannot be explained solely by the changes in SOC.[29,49] The increase in the rate of ISC is likely due to the increased electron accepting ability of the naphthalimide unit, the resulting decrease in the energy of the singlet CT state in **B** and a reduced energy gap between the singlet and triplet states. Another factor may be a surprising partial delocalisation of the electron density over the benzoate substituent, adding additional degrees of freedom to couple singlet and triplet manifolds. This illustrates that slight modification of electron accepting ligands allows for tuning the rate of intersystem crossing without significantly altering the excited state electron density distribution, which clearly cannot be explained solely by the strength of the SOC. The unexpected participation of the ester-group vibrations, which occur in the same region as those of the NAP-acceptor ligand, thus overlapping spectrally and spatially, points towards the important role of intramolecular vibrations in ISC (as has been previously observed for, for example, Re(I) complexes).[66] Furthermore, the addition of the phenyl-*N* low-frequency rotational mode (50–60 cm^{-1}) shared between the singlet and the triplet manifold may contribute significantly to the ISC reaction coordinate, increasing the rate of this process in **B** vs. its *N*-alkyl counterpart.

Expanding our repertoire of techniques into μs-TRIR measurements using synchronised picosecond excitation and a broadband femtosecond probe allowed us to directly obtain the signatures of the long-lived excited states in the mid-IR region, confirming their ligand-localised nature and obtaining IR signatures of the triplet state of the naphthalimide. Overall, this work provides further insight into the design of Pt(II) chromophores, emphasises the potential of fine-tuning their excited state properties by seemingly peripheral modifications, and reinforces the role of spin–vibronic effects[45,46] amongst the factors driving ultrafast intersystem crossing beyond spin–orbit coupling.

Experimental

Steady-state spectroscopy

UV-visible absorption spectroscopy measurements were performed using a Cary 50 Bio Spectrometer. Emission measurements were performed using a Cary Eclipse fluorometer. Both absorption and emission measurements were performed in a UV-fused quartz cell with a 10 mm pathlength. Fourier-transform infrared spectra were recorded using a PerkinElmer Spectrum One FT-IR spectrometer. Samples were measured in a liquid IR cell (Harrick Scientific) with CaF$_2$ windows with 2 mm thickness and a pathlength of 650 μm.

Fluorescence upconversion spectroscopy

Time-resolved broadband fluorescence upconversion (FLUP) spectroscopy experiments were performed in the Lord Porter Laser Laboratory at the University of Sheffield. The set-up is as described previously.[29]

A Ti:sapphire regenerative amplifier (Spitfire ACE PA-40, Spectra-Physics) that generates 800 nm pulses (40 fs FWHM, 10 kHz, 1.2 mJ) was used for excitation. 800 nm seed pulses (25 fs FWHM, 84 MHz) for the amplifier were generated using a Ti:sapphire oscillator (Mai Tai, Spectra-Physics). Two Nd:YLF lasers (Empower, Spectra-Physics) were used to pump the two amplification stages of the Spitfire ACE PA-40. Frequency doubling of the 800 nm output of the amplifier, in a β-barium borate crystal within a commercially available doubler/tripler (TimePlate, Photop Technologies), was used to generate 400 nm pump pulses (40 fs FWHM, 10 kHz, ∼0.3 μJ). The pump pulses were passed through a computer-controlled optical delay line (M-IMS400LM, Newport), translation of which gave control of time delay between pump and gate pulses, within a 4 ns window with a temporal resolution of 1.67 fs. The power of the pump pulses was controlled using a variable attenuation neutral-density filter wheel. Pump pulses were compressed in a double-pass two-prism compressor (AFS-FS Fused Silica Prism Pair, Thorlabs) to achieve minimal FWHM of a cross-correlation between the gate and pump pulses. Polarization was set to the magic angle, with respect to vertical, with a λ/2 plate. Pump pulses were then focused by a lens (*f* = 200 mm, fused silica) onto the sample cell, to a spot diameter of ≤0.1 mm. The 1320 nm gate pulses (80 fs FWHM, 10 kHz, 60 μJ) were generated by a traveling-wave optical parametric amplifier of superfluorescence (TOPAS prime, Light Conversion) pumped by the 800 nm (40 fs FWHM, 10 kHz, 0.5 mJ) output of the Ti:sapphire regenerative amplifier. The polarization of the gate pulses was set to horizontal using a wire-grid polariser in conjunction with a λ/2 plate. The wire-grid polarizer and λ/2 plate pair were used to attenuate the power of the gate pulses. Emission from the sample was collected in a forward-scattering geometry. A beam-stopper was used to block any transmitted pump light. The fluorescence was directed onto a 100 μm thick β-barium borate crystal (BBO crystal, EKSMA OPTICS) where it was upconverted by sum-frequency generation with 1320 nm gate pulses. The fluorescence and gate beams met at an angle of ∼21° at the crystal, in a spot of 0.6 mm diameter. Type II phase-matching was used in order to provide the broadest spectral window for upconversion.

The sample solution was placed in a fused silica cuvette with an internal path length of 1.0 mm and stirred with a magnetic stirrer.

Transient absorption spectroscopy in UV–NIR regions

Transient absorption measurements were performed in the Lord Porter Laser Laboratory at the University of Sheffield using HELIOS (Ultrafast Systems) spectrometer. A Ti:sapphire amplifier system (Spitfire ACE PA-40, Spectra Physics) was used to generate an 800 nm fundamental beam with a repetition rate of 10 kHz and a pulse duration of 40 fs. Excitation pulses were generated by a TimePlate by frequency doubling of the 800 nm fundamental beam. The white-light continuum was generated

This journal is © the Owner Societies 2025

Phys. Chem. Chem. Phys., 2025, **27**, 25825–25836 | **25833**

by focussing 2% of the 800 nm fundamental beam onto a rastered CaF_2 crystal with a thickness of 2 mm. The NIR probe was generated using a 17 mm sapphire crystal. The pump-on and -off pulses were obtained using a mechanical chopper set at a frequency of 2.5 kHz. Polarisation of the pump and probe beams was set to the magic angle, $54.7°$, using a $\lambda/2$ waveplate, to remove anisotropic contributions to the signal. After passing through the sample, the probe beam was collimated, and focussed onto a fibre-coupled spectrometer. The signal was detected using a CMOS detector for the UV-visible region and an InGaAs detector for the NIR region. The sample was placed in a fused silica cuvette with an internal path length of 1.0 or 2.0 mm. The sample solution was stirred with a magnetic stirrer.

Time-resolved infrared spectroscopy

Time-resolved infrared measurements were performed at ULTRA, the Central Laser Facility, STFC Rutherford Appleton Laboratory.[67] A Ti:sapphire regenerative amplifier (Thales) was used to generate 800 nm pulses, from which a mid-IR probe pulse was generated, with a 400 cm^{-1} bandwidth. Ultrafast infrared experiments were performed on samples in a liquid IR cell (Harrick Scientific) with 2 mm CaF_2 windows and a PTFE spacer (650 µm) in a flow system, used to prevent sample decomposition.

Microsecond time-resolved broadband infrared spectroscopy

Time-resolved broadband infrared spectroscopy measurements on the picosecond-to-microsecond timescale were performed in the Lord Porter Laboratory at the University of Sheffield. The µs-TRIR set-up is similar to the fs-TRIR set-up described previously.[68] A Ti:sapphire amplifier system (Spectra Physics, Spitfire Ace PA 100) was used to generate an 800 nm fundamental beam with an output of 14 W and 5 kHz (2.8 mJ), and a pule duration of 100 fs. A second-harmonic bandwidth compressor (Light Conversion) was used to generate a 400 nm pulse with a pulse duration of 5 ps (bandwidth of *ca.* 6 cm^{-1} at 400 nm). The pump pulses were delayed by an optical delay line, which has a maximum time delay of 11.8 ns. After this, the delays were generated using a digital delay generator (DDG) to achieve 3 µs steps to a maximum time delay of 50 µs. The Ti:sapphire regenerative amplifier (Spitfire ACE PA-40, Spectra Physics) was used to pump a commercial optical parametric amplifier (TOPAS, Light Conversion), which provided tuneable mid-IR pulses (2300–$10\,000 \text{ cm}^{-1}$, typical FWHM of $\sim 280 \text{ cm}^{-1}$) by difference frequency generation in GaSe. After the optical parametric amplifier (OPA), the probe beam passed through a Ge long pass filter and was collimated to a beam diameter of 10 mm in a two-mirror telescope.

The mid-IR beam was split into two using a CaF_2 beam splitter (50 : 50) to generate both probe and reference pulses. To focus the mid-IR pulse onto the sample, an off-axis parabolic mirror ($f = 211$ mm) was used. Pump polarisation was set to the magic angle ($54.7°$) to avoid the contributions of rotational relaxation to the sign and the pump pulse energy was set using a neutral density filter. The UV-vis pump was focussed onto the probe spot at the sample using an aluminium $90°$ off-axis parabolic mirror ($f = 100$ mm) to a spot-size of $\sim 300 \times 300$ µm^2. The probe spot size was $\sim 250 \times 250$ µm^2. Following the sample, a second parabolic mirror was used to collimate probe and reference beams, which were then split using a $50 : 50$ CaF_2 beam splitter to give two separate beams. The two beams were then focussed into two separate spectrometers (Horiba iHR320) and dispersed with a 50 mm^{-1} grating. The signals are then detected using two multichannel HgCdTe detectors (Infrared Associates), which are LN$_2$ cooled and composed of a total of 128 pixels, of which 96 are assigned to the probe and 32 to the reference.

Signal-to-noise was improved using multichannel referencing as described by Ge *et al.*[69,70] The B-matrix was calculated from the pump-off shots.

Samples were measured in solution in a liquid IR flow cell (Harrick Scientific) with two 2 mm CaF_2 windows and a PTFE spacer (650 µm). The cell was rastered in the x, y directions.

Calculations

The details of the DFT calculations are given in the SI.

Global analysis and data fitting

Single-point kinetic fits were carried out using OriginPro 2023. Global lifetime analysis was performed using MATLAB 2022a.

Conflicts of interest

There are no conflicts to declare.

Data availability

NMR and mass spectra are saved in the Chemistry archive. Raw data are available upon request. FTIR data are stored in accordance with the University of Sheffield data policy. The data are available as .csv files. Time-resolved infrared data, fluorescence upconversion data, and transient absorption data are available *via* the Lord Porter Laser Laboratory Google Drive and archives, stored in accordance with the University of Sheffield data policy. Further time-resolved infrared data recorded at the Laser for Science facility are saved on the facility's drives, as well as in the group repository. Computational output data are available through the University of Pennsylvania repository and from the co-author (Dr James Shipp). All source data are also available from the corresponding author Julia Weinstein.

The SI contains synthetic procedures and characterisation data, details of DFT calculations, and additional spectral information. See DOI: **https://doi.org/10.1039/d5cp02392k**.

Acknowledgements

25834 | *Phys. Chem. Chem. Phys.*, 2025, **27**, 25825–25836

This journal is © the Owner Societies 2025

References

1 S. Archer and J. A. Weinstein, *Coord. Chem. Rev.*, 2012, **256**, 2530–2561.

2 M. K. Nazeeruddin and M. Grätzel, *Struct. Bond.*, 2007, **123**, 113–175.

3 H. Kumagai, Y. Tamaki and O. Ishitani, *Acc. Chem. Res.*, 2022, **55**, 978–990.

4 K. Eastham, A. D. W. Kennedy, S. I. Scottwell, J. E. Bramham, S. Hardman, A. P. Golovanov, P. A. Scattergood, J. D. Crowley and P. I. P. Elliott, *Inorg. Chem.*, 2024, **63**, 9084–9097.

5 E. Baggaley, J. A. Weinstein and J. A. G. Williams, *Coord. Chem. Rev.*, 2012, **256**, 1762–1785.

6 K. K.-W. Lo, *Photofunctional Transition Metal Complexes*, Springer-Verlag, Berlin Heidelberg, 2006, pp. 205–245.

7 J. K. McCusker, *Science*, 2019, **363**, 484–488.

8 C. K. Prier, D. A. Rankic and D. W. C. MacMillan, *Chem. Rev.*, 2013, **113**, 5322–5363.

9 Y. Yamazaki, H. Takeda and O. Ishitani, *J. Photochem. Photobiol., C*, 2015, **25**, 106–137.

10 G.-J. Zhou and W.-Y. Wong, *Chem. Soc. Rev.*, 2011, **40**, 2541.

11 F. Guo, Y. G. Kim, J. R. Reynolds and K. S. Schanze, *Chem. Commun.*, 2006, 1887–1889.

12 J. Mei, K. Ogawa, Y.-G. Kim, N. C. Heston, D. J. Arenas, Z. Nasrollahi, T. D. McCarley, D. B. Tanner, J. R. Reynolds and K. S. Schanze, *ACS Appl. Mater. Interfaces*, 2009, **1**, 150–161.

13 J. S. Wilson, A. S. Dhoot, A. J. A. B. Seeley, M. S. Khan, A. Köhler and R. H. Friend, *Nature*, 2001, **413**, 828–831.

14 C. Liao, A. H. Shelton, K. Y. Kim and K. S. Schanze, *ACS Appl. Mater. Interfaces*, 2011, **3**, 3225–3238.

15 E. Glimsdal, M. Carlsson, B. Eliasson, B. Minaev and M. Lindgren, *J. Phys. Chem. A*, 2007, **111**, 244–250.

16 J. E. Rogers, J. E. Slagle, D. M. Krein, A. R. Burke, B. C. Hall, A. Fratini, D. G. McLean, P. Fleitz, T. M. Cooper, M. Drobizhev, N. S. Makarov, A. Rebane, K.-Y. Kim, R. Farley and K. S. Schanze, *Inorg. Chem.*, 2007, **46**, 6483–6494.

17 S. Fukuzumi, K. Ohkubo and T. Suenobu, *Acc. Chem. Res.*, 2014, **47**, 1455–1464.

18 M. R. Wasielewski, *Acc. Chem. Res.*, 2009, **42**, 1910–1921.

19 F. N. Castellano, *Acc. Chem. Res.*, 2015, **48**, 828–839.

20 A. J. Auty, P. A. Scattergood, T. Keane, T. Cheng, G. Wu, H. Carson, J. Shipp, A. Sadler, T. Roseveare, I. V. Sazanovich, A. J. H. M. Meijer, D. Chekulaev, P. I. P. Elliot, M. Towrie and J. A. Weinstein, *Chem. Sci.*, 2023, **14**, 11417–11428.

21 J. C. López-López, Y. H. Nguyen, C. Jiang and T. S. Teets, *Inorg. Chem.*, 2023, **62**, 17843–17850.

22 A. Molina-Ontoria, D. M. Rivera-Nazario, A. Tigreros, A. Ortiz, J. E. Nuñez, B. Insuasty, D. Lueders, S. Wolfrum, D. M. Guldi and L. Echegoyen, *Chem. – Eur. J.*, 2014, **20**, 11111–11119.

23 F. N. Castellano, I. E. Pomestchenko, E. Shikhova, F. Hua, M. L. Muro and N. Rajapakse, *Coord. Chem. Rev.*, 2006, **250**, 1819–1828.

24 C. J. Adams, N. Fey, Z. A. Harrison, I. V. Sazanovich, M. Towrie and J. A. Weinstein, *Inorg. Chem.*, 2008, **47**, 8242–8257.

25 M. Younus, S. Valandro, H. B. Gobeze, S. Ahmed and K. S. Schanze, *J. Photochem. Photobiol., A*, 2023, **435**, 114303.

26 P. A. Scattergood, M. Delor, I. V. Sazanovich, M. Towrie and J. A. Weinstein, *Faraday Discuss.*, 2015, **185**, 69–86.

27 M. W. Mara, N. P. Weingartz, D. Leshchev, D. Hsu, A. Valentine, A. Mills, S. Roy, A. Chakraborty, P. Kim, E. Biasin, K. Haldrup, M. S. Kirschner, D. Rimmerman, M. Chollet, J. M. Glownia, T. B. van Driel, F. N. Castellano, X. Li and L. X. Chen, *J. Phys. Chem. Lett.*, 2024, **15**, 5250–5258.

28 K. Choroba, J. Palion-Gazda, A. Kryczka, E. Malicka and B. Machura, *Dalton Trans.*, 2025, 2209–2223.

29 G. A. Farrow, M. Quick, S. A. Kovalenko, G. Wu, A. Sadler, D. Chekulaev, A. A. P. Chauvet, J. A. Weinstein and N. P. Ernsting, *Phys. Chem. Chem. Phys.*, 2021, **23**, 21652–21663.

30 P. Kim, A. J. S. Valentine, S. Roy, A. W. Mills, F. N. Castellano, X. Li and L. X. Chen, *Faraday Discuss.*, 2022, **237**, 259–273.

31 S. Kromer, S. Roy, J. E. Yarnell, C. M. Taliaferro and F. N. Castellano, *Dalton Trans.*, 2023, **52**, 4008–4016.

32 S. R. Valandro, R. He, J. D. Bullock, H. Arman and K. S. Schanze, *Inorg. Chem.*, 2021, **60**, 10065–10074.

33 E. O. Danilov, A. Rachford, S. Goeb and F. N. Castellano, *J. Phys. Chem. A*, 2009, **113**, 5763–5768.

34 B. A. Llewellyn, A. G. Slater, G. Goretzki, T. L. Easun, X.-Z. Sun, E. S. Davies, S. P. Argent, W. Lewis, A. Beeby, M. W. George and N. R. Champness, *Dalton Trans.*, 2014, **43**, 85–94.

35 R. Liang, W. Xiong, X. Bai, L. Du and D. L. Phillips, *J. Phys. Chem. C*, 2021, **125**, 11432–11439.

36 G. Ramakrishna, T. Goodson III, J. E. Rogers-haley, T. M. Cooper, D. G. Mclean and A. Urbas, *J. Phys. Chem. C*, 2009, **113**, 1060–1066.

37 R. M. van der Veen, A. Cannizzo, F. van Mourik, A. Vlček and M. Chergui, *J. Am. Chem. Soc.*, 2011, **133**, 305–315.

38 S. E. Brown-Xu, M. S. J. Kelley, K. A. Fransted, A. Chakraborty, G. C. Schatz, F. N. Castellano and L. X. Chen, *J. Phys. Chem. A*, 2016, **120**, 543–550.

39 J. E. Yarnell, I. Davydenko, P. V. Dorovatovskii, V. N. Khrustalev, T. V. Timofeeva, F. N. Castellano, S. R. Marder, C. Risko and S. Barlow, *J. Phys. Chem. C*, 2018, **122**, 13848–13862.

40 J. E. Yarnell, A. Chakraborty, M. Myahkostupov, K. M. Wright and F. N. Castellano, *Dalton Trans.*, 2018, **47**, 15071–15081.

This journal is © the Owner Societies 2025

Phys. Chem. Chem. Phys., 2025, **27**, 25825–25836 | **25835**

41 F. Zhong, J. Zhao, M. Hayvali, A. Elmali and A. Karatay, *Inorg. Chem.*, 2019, **58**, 1850–1861.

42 L. Mewes, R. A. Ingle, S. Megow, H. Böhnke, E. Baranoff, F. Temps and M. Chergui, *Inorg. Chem.*, 2020, **59**, 14643–14653.

43 A. J. S. Valentine, J. J. Radler, A. Mills, P. Kim, F. N. Castellano, L. X. Chen and X. Li, *J. Chem. Phys.*, 2019, **151**(11), 114303.

44 C. M. Marian, *Annu. Rev. Phys. Chem.*, 2020, **72**, 617–640.

45 S. Mandal and C. Daniel, *Phys. Chem. Chem. Phys.*, 2023, **25**, 18720–18727.

46 S. Mandal and C. Daniel, *J. Phys. Chem. A*, 2024, **128**, 3126–3136.

47 S. Cho, M. W. Mara, X. Wang, J. V. Lockard, A. Rachford, F. N. Castellano and L. X. Chen, *J. Phys. Chem. A*, 2011, **115**, 3990–3996.

48 H. Guo, M. L. Muro-Small, S. Ji, J. Zhao and F. N. Castellano, *Inorg. Chem.*, 2010, **49**, 6802–6804.

49 P. A. Scattergood, M. Delor, I. V. Sazanovich, O. V. Bouganov, S. A. Tikhomirov, A. S. Stasheuski, A. W. Parker, G. M. Greetham, M. Towrie, E. S. Davies, A. J. H. M. Meijer and J. A. Weinstein, *Dalton Trans.*, 2014, **43**, 17677–17693.

50 F. Zhong and J. Zhao, *Eur. J. Inorg. Chem.*, 2017, 5196–5204.

51 L. Liu, D. Huang, S. M. Draper, X. Yi, W. Wu and J. Zhao, *Dalton Trans.*, 2013, **42**, 10694–10706.

52 Z.-L. Gong, Q.-J. Pan, D.-X. Ma and Y.-W. Zhong, *Inorganics*, 2023, **11**, 438.

53 S. Zhu, H. Liu, K. Wang, Q. Cheng, Z. Ma, R. Liu, G. Song and H. Zhu, *Dalton Trans.*, 2019, **48**, 15105–15113.

54 J. A. Weinstein, D. C. Grills, M. Towrie, P. Matousek, A. W. Parker and M. W. George, *Chem. Commun.*, 2002, 382–383.

55 G. R. Fleming and M. Cho, *Annu. Rev. Phys. Chem.*, 1996, **47**, 109–134.

56 M. L. Horng, J. A. Gardecki, A. Papazyan and M. Maroncelli, *J. Phys. Chem.*, 1995, **99**, 17311–17337.

57 I. V. Sazanovich, M. A. H. Alamiry, A. J. H. M. Meijer, M. Towrie, E. S. Davies, R. D. Bennett and J. A. Weinstein, *Pure Appl. Chem.*, 2013, **85**, 1331–1348.

58 I. V. Sazanovich, J. Best, P. A. Scattergood, M. Towrie, S. A. Tikhomirov, O. V. Bouganov, A. J. H. M. Meijer and J. A. Weinstein, *Phys. Chem. Chem. Phys.*, 2014, **16**, 25775–25788.

59 M. Delor, I. V. Sazanovich, M. Towrie and J. A. Weinstein, *Acc. Chem. Res.*, 2015, **48**, 1131–1139.

60 E. A. Glik, S. Kinayyigit, K. L. Ronayne, M. Towrie, I. V. Sazanovich, J. A. Weinstein and F. N. Castellano, *Inorg. Chem.*, 2008, **47**, 6974–6983.

61 S. A. Archer, T. Keane, M. Delor, E. Bevon, A. J. Auty, D. Chekulaev, I. V. Sazanovich, M. Towrie, A. J. H. M. Meijer and J. A. Weinstein, *Chem. – Eur. J.*, 2017, **23**, 18239–18251.

62 M. Delor, S. A. Archer, T. Keane, A. J. H. M. Meijer, I. V. Sazanovich, G. M. Greetham, M. Towrie and J. A. Weinstein, *Nat. Chem.*, 2017, **9**, 1099–1104.

63 J. D. Shipp, R. J. Fernández-Terán, A. J. Auty, H. Carson, A. J. Sadler, M. Towrie, I. V. Sazanovich, P. M. Donaldson, A. J. H. M. Meijer and J. A. Weinstein, *ACS Phys. Chem. Au*, 2024, **4**, 761–772.

64 E. Pomarico, P. Pospíšil, M. E. F. Bouduban, J. Vestfrid, Z. Gross, S. Záliš, M. Chergui and A. Vlček, *J. Phys. Chem. A*, 2018, **122**, 7256–7266.

65 I. V. Sazanovich, M. A. H. Alamiry, J. Best, R. D. Bennett, O. V. Bouganov, E. S. Davies, V. P. Grivin, A. J. H. M. Meijer, V. F. Plyusnin, K. L. Ronayne, A. H. Shelton, S. A. Tikhomirov, M. Towrie and J. A. Weinstein, *Inorg. Chem.*, 2008, **47**, 10432–10445.

66 A. El Nahhas, C. Consani, A. M. Blanco-Rodríguez, K. M. Lancaster, O. Braem, A. Cannizzo, M. Towrie, I. P. Clark, S. Záliš, M. Chergui and A. Vlček, *Inorg. Chem.*, 2011, **50**, 2932–2943.

67 G. M. Greetham, P. Burgos, Q. Cao, I. P. Clark, P. S. Codd, R. C. Farrow, M. W. George, M. Kogimtzis, P. Matousek, A. W. Parker, M. R. Pollard, D. A. Robinson, Z.-J. Xin and M. Towrie, *Appl. Spectrosc.*, 2010, **64**, 1311–1319.

68 M. V. Appleby, R. A. Cowin, I. I. Ivalo, S. L. Peralta-Arriaga, C. C. Robertson, S. Bartlett, A. Fitzpatrick, A. Dent, G. Karras, S. Diaz-Moreno, D. Chekulaev and J. A. Weinstein, *Faraday Discuss.*, 2023, **244**, 391–410.

69 Y. Feng, I. Vinogradov and N.-H. Ge, *Opt. Express*, 2017, **25**, 26262.

70 Y. Feng, I. Vinogradov and N.-H. Ge, *Opt. Express*, 2019, **27**, 20323.

25836 | *Phys. Chem. Chem. Phys.*, 2025, **27**, 25825–25836

This journal is © the Owner Societies 2025